#### **ORIGINAL ARTICLE**



# Investigation of surface roughness, microstructure, and mechanical properties of overhead structures fabricated by wire + arc additive manufacturing

Sainand Jadhav<sup>1</sup> · Gwang Ho Jeong<sup>2</sup> · Mahdi Sadeqi Bajestani<sup>1</sup> · Saiful Islam<sup>1</sup> · Ho-Jin Lee<sup>3</sup> · Young Tae Cho<sup>2</sup> · Duck Bong Kim<sup>4</sup>

Received: 24 November 2023 / Accepted: 19 February 2024 © The Author(s), under exclusive licence to Springer-Verlag London Ltd., part of Springer Nature 2024

#### **Abstract**

This study aims to investigate surface roughness, microstructure, and mechanical properties of overhead thin-wall structures of stainless steel(SS316L) fabricated by cold metal transfer (CMT)-based wire + arc additive manufacturing (WAAM). In the first stage, single-layer bead experiments were carried out in flat and overhead positions utilizing Box-Behnken experimental design with a range of process parameters (i.e., wire feed rate, travel speed, and weave amplitude). To study the effect of individual process parameters on the bead geometry and identify a process window, analysis of variance(ANOVA) is performed using the bead cross-section measurement data. For single layer bead experiments in flat and overhead position, out of all process parameters, the weave amplitude is the most significant parameter on bead width, whereas travel speed is most significant parameter for bead height. Based on single-layer bead experiments, process parameters for thin wall deposition were identified. In the second stage, two thin-walls were deposited with wire feed rates of 1000 and 1500 mm/min in the overhead position. The surface roughness was measured using cloud point data acquired from the coordinate measuring machine(CMM). The deposited structure with the wire feed rate of 1500 mm/min resulted in better surface quality. It was also observed that, microstructure was composed of austenite and dendritic delta ferrite. The microstructure changed as the deposition height increased. The average microhardness value was measured 183 HV and 187.4 HV for the overhead structures. Average tensile properties of the SS316L overhead structures were comparable to that of SS316L fabricated by other WAAM processes.

 $\textbf{Keywords} \ \ \text{Overhead structures} \cdot \text{Wire} + \text{Arc additive manufacturing} \cdot \text{Experimental design} \cdot \text{Surface roughness} \cdot \text{Microstructure}$ 

□ Duck Bong Kim dkim@tntech.edu

Published online: 01 March 2024

- Department of Mechanical Engineering, Tennessee Technological University, Cookeville, TN, USA
- Department of Smart Manufacturing Engineering, Changwon National University, Changwon, South Korea
- Extreme Fabrication Technology Group, Korea Institute of Industrial Technology, 350-27, Gumi-daero, Gumi-si, Gyeongsang buk-do 39253, South Korea
- Department of Manufacturing and Engineering Technology, Tennessee Technological University, Cookeville, TN, USA

# 1 Introduction

Additive manufacturing (AM) is the process of joining materials to make parts from a 3D model through the layer-by-layer stacking mechanism. It offers a broad range of new opportunities to design and fabricate geometrically complex metallic components with a low buy-to-fly ratio [1]. AM processes can be categorized as binder jetting, material extrusion, material jetting, sheet lamination, vat photopolymerization, powder bed fusion (PBF), and directed energy deposition (DED) [2]. Among them, PBF and DED are the most widely investigated metal AM processes. PBF has the capability of fabricating parts with high geometric accuracy. However, it has the limitation of building volume along with a slower deposition rate



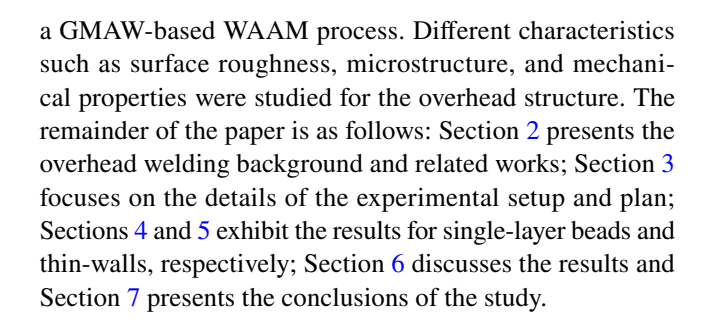
of 10 g/min, making it infeasible to fabricate larger components [3, 4]. In addition, it requires support structures to be removed after the part is manufactured, which increases material cost, wastage, and production time.

DED, the other prevalent AM process, can be classified into powder-feed and wire-feed systems [5]. The latter can be further categorized with respect to the energy sources, such as laser, electron, and welding arc [6]. Wire+arc additive manufacturing (WAAM) utilizes a welding arc as the energy source to melt and deposit the final structure. It can be further divided into gas metal arc welding (GMAW), plasma arc welding (PAW), and gas tungsten arc welding (GTAW), based on the type of heat sources utilized [7]. The benefits of WAAM compared to other techniques include a high deposition rate, low material cost, low capital cost of setup and maintenance, and high material utilization [8]. These unique characteristics provide WAAM with the feasibility to produce large-scale metal parts.

Metal AM processes that can be applied to large-scale manufacturing have received increased attention recently. Among large-scale AM, parts having their longest axis length at a minimum of 1-2 m are called metal big area additive manufacturing (mBAAM), and can be widely used in automotive and aerospace industries [9]. For example, "Relativity Space" launched the space rocket called "Terran 1" whose body (e.g., propellant tank) was mainly fabricated by WAAM [10]. The rocket was produced with 100 times fewer parts within 60 days using artificial intelligence (AI)based design and AM technology. In this context, the ability to fabricate inclined, overhead, and overhang structures are prerequisite for the mBAAM applications to incorporate flexibility for complicated structures. This will significantly reduce the time and cost, as well as increase manufacturing freedom by eliminating the requirement of support structure.

In terms of the hardware configuration for WAAM processes, for moving the torch, usually a 3-axis CNC router or a 6-axis welding robot is used [6]. Generally, a turntable in WAAM has 1 or 2-axis. More axes provide more flexibility for fabricating complex geometries, yet limit the size of the parts to be manufactured. For example, the bending moment is huge for large components in the case of the 2-axis turntable. Accordingly, from the large-scale metal AM perspective, the 6-axis robot and 1-axis turn table hardware combination is the best option considering the process scalability, system cost, and part mass [6, 11, 12]. Contrary to the PBF process, fabricating overhead and overhang structures using WAAM does not necessitate support structures if proper hardware configurations and processes are applied. However, the knowledge in this area is significantly lacking, and the application of WAAM for fabricating the overhead structures has not been thoroughly investigated.

In this study, we investigated the feasibility of fabricating the stainless steel (SS) 316L overhead thin-walls using



# 2 Background and related work

This section will discuss the research on fabricating different structures using WAAM, including vertical, inclined, near horizontal, and overhead. The studies regarding surface roughness, weld pool behavior, and acting forces in the cold metal transfer (CMT) process are comprehensively reported.

#### 2.1 WAAM for thin-wall structures

Feasibility of WAAM for different materials has been investigated by the researchers. Chakkravarthy and Jerome [13] investigated the influence of torch angle on texture, orientation, and topology in CMT for SS 316L. They observed that the heat input considerably increased with the torch angle increasing from 5° to 15°. Xie et al. [14] employed a single-channel multilayer continuous deposition method based on the CMT plus pulse process to fabricate SS 316L thin-walls. They concluded that along the building direction, the alloy in different regions solidified in a ferritic-austenitic manner, and due to different heat histories, their microstructures were significantly distinct. The ultimate tensile strength (UTS) and yield strength (YS) of the vertical specimens were higher than those of the horizontal specimens, displaying the anisotropy.

The AM community has also investigated inclined and near horizontal structures. Xiong et al. [15] researched the limits of producing inclined, thin-wall features with flat position deposition by keeping the welding torch normal to the substrate. Panchagnula et al. [16] proposed an inclined slicing technique to manufacture dense near-net metallic components without support structures employing GMAW-based metal AM. Zhao et al. [17] developed a statistical prediction model to explain the dependence of the inclination angle of thin-walls on process parameters such as wall width, offset distance, wire feed rate (WFR), and travel speed (TS) in CMT-WAAM. Li et al. [18] presented a method to fabricate curved, overhanging thin-walls without using turn tables and support structures to unlock the potential of the 6-axis industrial robots. They used the torch orientation to control the weld pool flow. As the literature suggests, no research has focused on fabricating overhead structures using WAAM. Considering their numerous applications in the industry,



especially in the case of large-scale metal additive manufacturing, this knowledge gap will be addressed in this study. The following subsection will elaborate on the challenges of overhead WAAM by reviewing the related literature.

#### 2.2 Overhead welding

The American Welding Society (AWS) classified four primary welding positions: flat position (1F/1G), horizontal position (2F/2G), vertical position (3F/3G), and overhead position(4F/4G) [19]. One major issue in the overhead welding position is the metal sagging, which results in a crownshaped deposition. This issue may be avoided by keeping the molten metal small. In the case of overhead welding, gravity influences the welding performance, which affects weld pool behavior; hence, it is necessary to understand the effect of gravity on the weld pool. To investigate this, Nguyen et al. [20] studied the effects of gravity numerically in main welding configurations. It was concluded that gravity mainly acts on the weld pool shape, whereas Marangoni and Lorentz forces drive the fluid flow. The thermal field is only slightly impacted by the different positions (only 5% between flat and vertical-up cases). In addition, gravity pulls the liquid metal from the upper toward lower melted pool regions, so the weld pool surface deforms in the gravity direction, negatively influencing the stability of the bead shape in the overhead position.

Park et al. [21] performed welding on flat, overhead, and vertical welding positions using the pulsed-GMAW process. They observed weld pool behavior and analyzed their microstructures. In the overhead position, due to the reverse gravity direction combined with the backward flow, the tail of the weld pool increased the bead height, resulting in a convex-shaped bead. Yaakub et al. [22] predicted welding parameters and bead geometry for the GMAW process in an overhead T-fillet welding position (4F). They established a correlation between bead geometry and heat input and developed a bead geometry predictor. Kang et al. [23] performed welds in different gravity directions, such as vertical up position, vertical down position, and flat position. The vertical up position caused 21% deeper penetration than the vertical down position. Kang et al. [24] stated that the direction of gravity significantly influences the weld pool shape associated with convection flows, which affects the solidification morphology and the primary dendrite spacing.

# 2.3 Weld pool behavior and forces in CMT

Numerous studies have investigated the weld pool behavior and forces in CMT for different materials and process parameters. Hu et al. [25] developed a computational fluid dynamics model of the weld pool considering the droplet impingement, gravity, arc force, heat, and mass transfer for four typical welding positions. Murphy [26] applied a unique approach to model a GMAW process with a 3D model. He employed an equilibrium surface method to track the free surface of the melt pool. Ogino and Hirata [27] proposed a 3D model to simulate droplets and arc plasma interactions. In addition, Ogino et al. [28] compared shielding gases of argon and an argon-CO<sub>2</sub> mixture and found that the nature of the gas influences the detachment frequency and temperature of the droplets. Zhao and Chung [29] developed a coupled magneto-hydrodynamic model to study metal transfer and heat transfer behavior in the GMAW process using an alternative current.

The forces acting on the weld pool in the GMAW process are gravity, buoyancy, electromagnetic, surface tension, Marangoni, and arc pressure [30]. During the CMT short-circuit phase, various forces generated by welding wire motion act on a droplet, such as gravity, surface tension, electromagnetic force, and pulling force [31–33]. Gravity influences welding performance and the weld pool behavior; hence, it is necessary to understand its effects on the dimensions, microstructure evolution, and mechanical properties of the weld structure. However, to the best of our knowledge, little research has been conducted regarding the effect of gravity on the microstructural evolution and mechanical properties of the structures manufactured by the overhead welding process.

# 2.4 Surface roughness in WAAM

Controlling surface roughness is one of the challenges in the WAAM processes. The surface roughness studies can be categorized into the top and side surface roughness evaluation [34–36]. Both are important since they will affect the properties of the final product. Yehorov et al. [37] evaluated the side surface waviness of thin-walls produced by different currents, WFR, and TS. They concluded that a suitable TS range could enhance surface roughness. Li et al. [38] developed a WAAM process to manufacture a thin-wall with a side surface roughness of about 5 µm, which is much better than other research methods. However, they used small-power metal fine wire feeding, which is not feasible for most AM of large parts. Xiong et al. [15] proposed a methodology based on a laser vision system to quantify the surface roughness of the multilayer single-pass low-carbon steel thin-walls deposited by GMAW-based AM. They concluded that surface roughness is closely related to wire feeding and scanning speeds, welding current mode, cooling time, and interpass temperature.

# 3 Experimental setup and plans

#### 3.1 Experimental setup

The in-house developed WAAM setup was used for this study, as shown in Fig. 1 [3]. The system comprises an



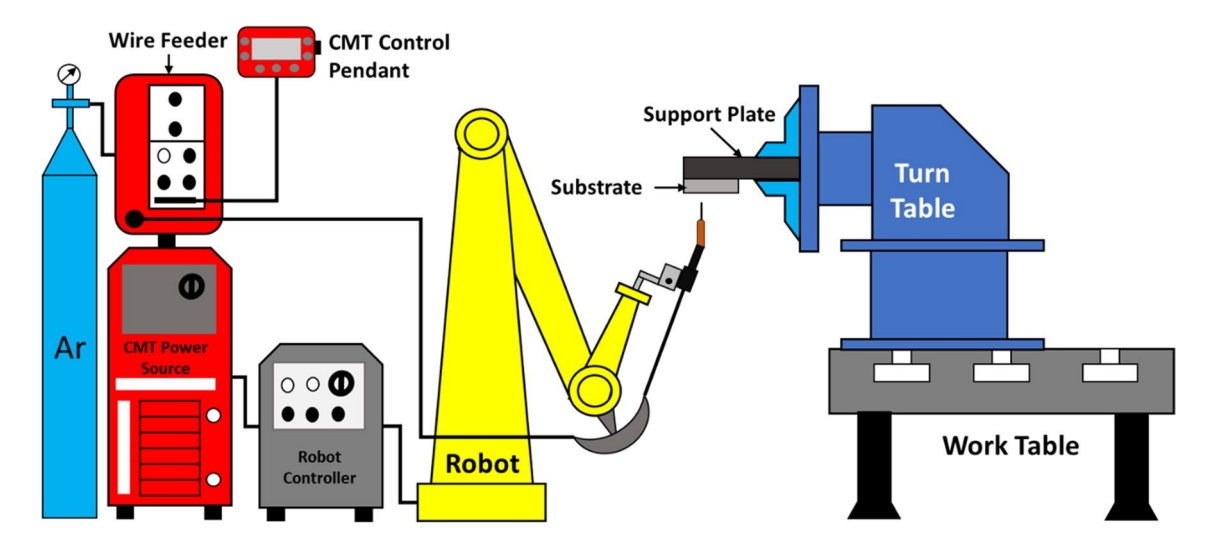


Fig. 1 Experimental setup with fixture for fabricating the overhead structure

**Table 1** Elemental composition (wt.%) of SS 316L

Elements	С	Mn	Si	S	P	Cr	Ni	Мо	Cu	N	Fe
Composition (wt.%)	0.02	2.1	0.81	0.01	0.02	18.9	11.8	2.2	0.23	0.05	Bal

Advanced 4000MVR CMT machine, a VR7000 wire feeder, and a six-axis Fanuc ArcMate 120iC robot with a controller (Fanuc R-30iA). The TS, welding current and voltage, WFR, and weave amplitude (WA) were controlled throughout the process. Miller Insight ArcAgent Auto with Miller Centerpoint software was used to acquire process signatures, such as current and voltage. SS 316L wire with a diameter of 1.2 mm was used in this experiment, and its elemental composition is shown in Table 1. An SS 316L plate with dimensions of  $150 \times 50 \times 6$  mm³ was used as the substrate. It was clamped to the support plate using C-clamps, and the support plate was held in the chuck of the turn table. The surface of the substrate was polished and cleaned with acetone before the deposition.

# 3.2 Experimental plan for single-layer beads

The CMT torch was given a weaving path during the deposition of single-layer beads and thin-walls. At first, single-layer beads were produced utilizing the constant parameters as shown in Table 2. Three levels were chosen for each of the parameters, WFR, TS, and WA. The Box-Behnken design of experiment method was used to determine the influence of process parameters on the output variables and their interactions. The ranges of the process parameters were determined based on preliminary investigations. Heat input and energy density were calculated using Eqs. (1) and (2). For each condition, the current and voltage was obtained from the monitoring system. Table 3 summarizes the Box-Behnken

**Table 2** Constant process parameters that were not varied during the deposition

Process parameters	Value		
Contact tip to work distance (CTWD)	12 mm		
Torch angle	90°		
Diameter of the consumable wire	1.2 mm		
Shielding composition	100% Ar		
Shielding gas flow rate	20 L min <sup>-1</sup>		
Substrate material	SS 316L		
Interpass temperature	40 °C		
Weave frequency	2 Hz		

design of experiment with the associated heat input and energy density in each condition.

$$Heat input\left(\frac{J}{mm}\right) = \frac{Current \times Voltage}{TS/60} \tag{1}$$

Energy Density 
$$\left(\frac{J}{mm^3}\right) = \frac{Current \times Voltage}{\pi \times (radius \ of \ wire)^2 \times WFR/60}$$
 (2)

#### 3.3 Experimental plan for thin-walls

The parameters for depositing overhead thin-walls were selected based on the result of single-layer experiments.



Table 3 Box-Behnken design and the calculated heat input and energy density for each condition

Expt. No.	WFR (mm/min)	TS (mm/min)	WA (mm)	WFR / TS	Heat input (J/mm)		Energy Density (J/mm <sup>3</sup> )		
					Overhead	Flat	Overhead	Flat	
C1	1000	70	4	14.28	678.41	759.86	10.50	11.76	
C2	1000	160	5	6.25	301.51	307.74	10.66	10.88	
C3	1000	160	3	6.25	304.37	321.12	10.76	11.36	
C4	1000	250	4	4.00	193.17	185.84	10.67	10.27	
C5	1500	70	3	21.43	904.26	998.51	9.33	10.30	
C6	1500	70	5	21.43	794.69	865.58	8.20	8.93	
C7	1500	160	4	9.38	336.98	382.13	7.94	9.01	
C8	1500	160	4	9.38	350.54	366.87	8.26	8.65	
C9	1500	160	4	9.38	334.36	382.19	7.88	9.01	
C10	1500	250	3	6.00	219.36	240.00	8.08	8.84	
C11	1500	250	5	6.00	213.12	229.00	7.85	7.98	
C12	2000	70	4	28.57	1068.05	1196.32	8.26	9.25	
C13	2000	160	5	12.50	411.30	443.89	7.27	7.85	
C14	2000	160	3	12.50	430.88	475.70	7.62	8.41	
C15	2000	250	4	8.00	285.26	289.10	7.88	7.99	

The CMT process is based on a synergistic program for a particular material. The machine selects the welding current and voltage according to WFR using the synergic program [3, 39]. So, to keep current and voltage supplied by CMT machine constant during deposition of each layer, the thin walls were fabricated with constant WFR for each layer. Table 4 shows layer-wise process parameters for the deposition of two thin-walls. These two thin-walls were deposited with constant WFR of 1000 mm/min and 1500 mm/min, comprising 11 and 14 layers, respectively. However, TS and WA were varied on a layer-by-layer basis because the molten metal sags due to gravity during the deposition process. This

leads to the reduction of thin-wall thickness [refer Fig. 8a and e]. For the first 3 to 4 layers, the ratio of WFR to TS was ~ 15, and the WA was 5 mm; for the next 4 layers WFR/TS ratio was 10 while WA was reduced to 4.5 mm, and in the subsequent 4 layers, WFR/TS ratio was 8.33 and WA was 4 mm. WA is reduced by 0.5 mm after depositing a certain number of layers (3 to 4), and TS is increased (i.e., the WFR/TS ratio is reduced). WA is reduced to account for layer by layer reduction wall in thickness, whereas TS was increased to reduce sagging of molten metal. After the deposition of each layer, the deposited layer was allowed to cool down to 40 °C before depositing the next layer. The temperature was

**Table 4** Layer-wise process parameters for the thin-walls

	Thin-wall 1 (WF)	R 1000 mm/m	nin)	Thin-wall 2 (WFR 1500 mm/min)				
Layer	TS (mm/min)	WA (mm)	WFR /TS	TS (mm/min)	WA (mm)	WFR /TS		
1	70	5.0	14.28	100	5.0	15		
2	70	5.0	14.28	100	5.0	15		
3	70	5.0	14.28	100	5.0	15		
4	100	4.5	10.00	100	5.0	15		
5	100	4.5	10.00	150	4.5	10		
6	100	4.5	10.00	150	4.5	10		
7	100	4.5	10.00	150	4.5	10		
8	120	4.0	8.33	150	4.5	10		
9	120	4.0	8.33	180	4.0	8.33		
10	120	4.0	8.33	180	4.0	8.33		
11	120	4.0	8.33	180	4.0	8.33		
12	_	_	_	180	4.0	8.33		
13	_	_	_	180	3.5	8.33		
14	_	_	_	180	3.5	8.33		



measured by a hand-held device with a type K thermocouple by placing it on the surface of the deposited layer.

# 3.4 Microstructure and mechanical properties of the thin-walls

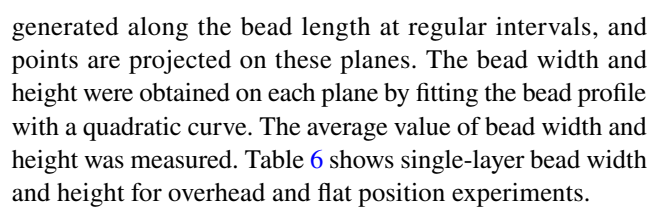
Microstructure and microhardness characterization samples were cut by wire electrical discharge machining (EDM) from the overhead thin-walls. They were ground and polished, following the general metallography procedure. Samples were ground coarsely using metallographic sandpaper with grit sizes 160, 360, and 600. After that, polishing was performed with a sequence of 3 μm and 1 μm polycrystalline diamond suspensions. Glyceregia solution (3 parts of HCl, 2 parts of glycerol, and 1 part of HNO<sub>3</sub>) was used for etching. The etched samples were observed using Nikon SMZ 1500 (magnification of 10X) and Nikon MA1500 (magnification of 1000X) optical microscope (OM). FEI Quanta 200 scanning electron microscope (SEM) with an energy-dispersive X-ray spectroscopy (EDS) attachment was used for microstructural and chemical composition analysis.

The mechanical performances of thin-walls were investigated through the computer-controlled, uniaxial tensile testing system (TestResources 810 E4 Electrodynamic Test Machine). The gauge section of the tensile sample is  $11 \times 3 \times 2$  mm<sup>3</sup>. Two samples in the build direction and two in the deposition direction were tested from each thin-wall with a strain rate of 0.01 mm/s. The fractured locations, surfaces, and modes were investigated using SEM to determine the failure characteristics and evaluate the presence of anomalies. Microhardness tests were performed along the build direction at 1 mm intervals from bottom to top with a 500 g load (Vickers diamond indenter) and a dwell time of 10 s. The tests were conducted using a Buehler Wilson VH1202 microhardness tester machine with an integrated high-resolution camera and DiametTM software.

# 4 Results for single-layer beads

Table 5 shows the images of 15 single-layer beads for overhead and flat positions. Visual inspections show that C2, C4, C10, C11, and C15 are abnormal, and the remaining beads are normal. For abnormal conditions, the heat input was 301.51, 193.17, 219.36, 213.12, and 285.26 J/mm which are relatively low.

To measure bead width and height, beads were scanned using Hexagon 7725SEI-4 Roamer Absolute Arm equipped with PCDMIS software. Point cloud data obtained by the line-structured light vision sensor reveals the three-dimensional (3D) shape of the single-layer bead. The data is imported into CloudCompare software to segment and slice the single-layer bead. Then, cross-section planes are



To study the effect of individual process parameters on the bead geometry and identify a process window for the single-layer beads in overhead and flat positions, analysis of variance (ANOVA) is performed using the bead crosssection measurement data, as presented in Table 6. Minitab software (version 17) has been used for the analysis. Figure 2a summarizes the main effect plot for the bead width in both flat and overhead positions. The mean values are indicated by dashed lines. The figure shows that the bead width has a positive correlation with WA for both conditions, suggesting it increases with the increase of WA. This is due to the wider side-to-side motion, which spreads the molten metal more evenly across the layer. In overhead conditions, bead width decreases with the WFR of 1000 to 1500 mm/min and then increases at the WFR of 2000 mm/ min. Similarly, it declines at the TS of 70 to 160 mm/min followed by an increase at 250 mm/min. Bead width results for flat positions are also consistent with these findings. As a result, WFR and TS has mixed effect on bead width of single layer beads in flat and overhead position.

Figure 2b shows the main effect plot for the bead height. The dashed line indicates the mean height values of the deposited beads. Bead height in the overhead position increases with the increase of WFR. On the contrary, the bead height decreases with increased TS. Figure 2b indicates that, TS is the most influential factor that controls bead height. The total amount of deposited material decreases with increasing TS, so the bead height decreases. Bead height also decreases with the increase of WA as the same amount of material is being deposited on a larger surface area. Similar results are also observed for the flat conditions. However, the average bead height in overhead conditions is higher compared to the flat position. This is due to the effect of gravity force along the build direction in overhead conditions.

Figure 3 explains the effect of heat input and energy density on the bead width and bead height. From Fig. 3a, it is evident that, for both deposition strategies, there is no strong correlation among bead width with heat input and energy density. The points are randomly distributed with respect to the mean values. From the main effect plot in Fig. 2a, it has been found that, the most significant parameter for bead width is WA. Both heat input and energy density do not depend on WA. As a result, no trend is observed among bead width with heat input and energy density. However, there is a positive correlation between the heat input and bead height as shown in Fig. 3b. From Fig. 2b, it has been found that, significant



Table 5 Image of single-layer beads for overhead and flat position experiments

Exp. No	o. Overhead position	Flat position	Normal (N) / Abnormal (A)
C1		Contract of the contract of th	N
C2	Calculation Cardio	The state of the s	A
C3	both confuture action buttenful town institutions	Contribution of confidences of the second sections	N
C4	(公司的公司的公司)		A
C5	AND THE PROPERTY OF THE PARTY O	Camer consistent and since the constitution of the	N
C6	The state of the s	for service and an analysis of the control of the c	N
C7	Months from the boils of the particular and a second	CONTRACTOR OF STREET ASSOCIATION OF STREET	N
C8	(Market and Substant By to an arm on the	Commence of the sections for the sections	N
С9	Commence of the state of the st		N
C10		Charles Handre Administration O	A
C11	CHINE THE PROPERTY OF THE PARTY		A
C12			N
C13	and designation of the second second second	Contra similari dika kacamatan C	N
C14	The same recover to the following of the section on the continuous contractions	(algunialities la linguisse as albumas en S	N
C15	<u>2cm</u>	2cm	A

factor for bead height is TS. As the TS decreases, the bead height increases. Heat input increases with the decrease of TS as shown in Eq. (2). This leads to a positive correlation between heat input and bead height. However, there is no clear correlation between energy density and bead height, which is confirmed by the random distribution of the data points.

# 5 Results for thin-walls

# 5.1 Deposited structure and 1D process signatures

Figure 4 shows the thin-walls deposited in the overhead position. The first layer deposition length is 112 mm in

both walls. It has been measured 71 mm and 76 mm for the last layer which indicates that deposition length decreased continuously with the increase of build height. This led to tapered shape of the walls at the deposition (arc) stop locations. The wall height is not uniform due to the humping effect. The heights of the thin-walls from the substrate are 39 mm and 37 mm at the deposition start location for thin-wall 1 and 2 respectively. It is also evident that surface roughness is significant in the deposited structures.

Figure 5 shows the layer-wise average current signature for the overhead structures. The total number of layers for deposits 1 and 2 were 11 and 14 respectively. For thin-wall 1, in the first and second layer, current signature remains approximately constant with no major fluctuation in the



**Table 6** Bead width and height of single-layer beads in the overhead and flat positions

Expt. No.	Overhead	d position			Flat position					
	Bead wid	dth (mm)	Bead height (mm)		Bead wid	dth (mm)	Bead height (mm)			
	Mean	Std. Dev.	Mean	Std. Dev.	Mean	Std. Dev.	Mean	Std. Dev.		
C1	9.052	0.196	4.433	0.132	10.687	0.187	3.954	0.136		
C2	10.616	0.234	2.784	0.190	11.072	0.167	2.568	0.100		
C3	6.697	0.212	2.704	0.204	7.364	0.652	2.742	0.218		
C4	11.871	2.117	1.196	0.181	13.995	3.584	1.201	0.187		
C5	8.956	0.280	5.550	0.518	10.972	0.283	4.788	0.150		
C6	11.488	0.260	4.243	0.152	13.312	0.396	3.823	0.142		
C7	8.759	0.255	2.684	0.140	9.448	1.324	2.681	0.245		
C8	8.730	0.262	2.681	0.158	10.045	3.779	2.690	0.255		
C9	8.210	0.350	2.688	0.186	8.691	0.773	2.611	0.246		
C10	6.282	0.480	2.284	0.367	6.256	0.443	2.446	0.20		
C11	10.804	0.180	2.564	0.128	11.096	0.252	2.470	0.128		
C12	10.593	0.475	5.048	0.432	12.872	0.374	4.718	0.288		
C13	11.113	0.628	2.380	0.187	14.084	2.331	1.998	0.186		
C14	8.386	2.271	3.800	0.404	9.192	0.141	2.797	0.094		
C15	9.277	1.193	1.936	0.300	9.686	1.273	1.783	0.254		

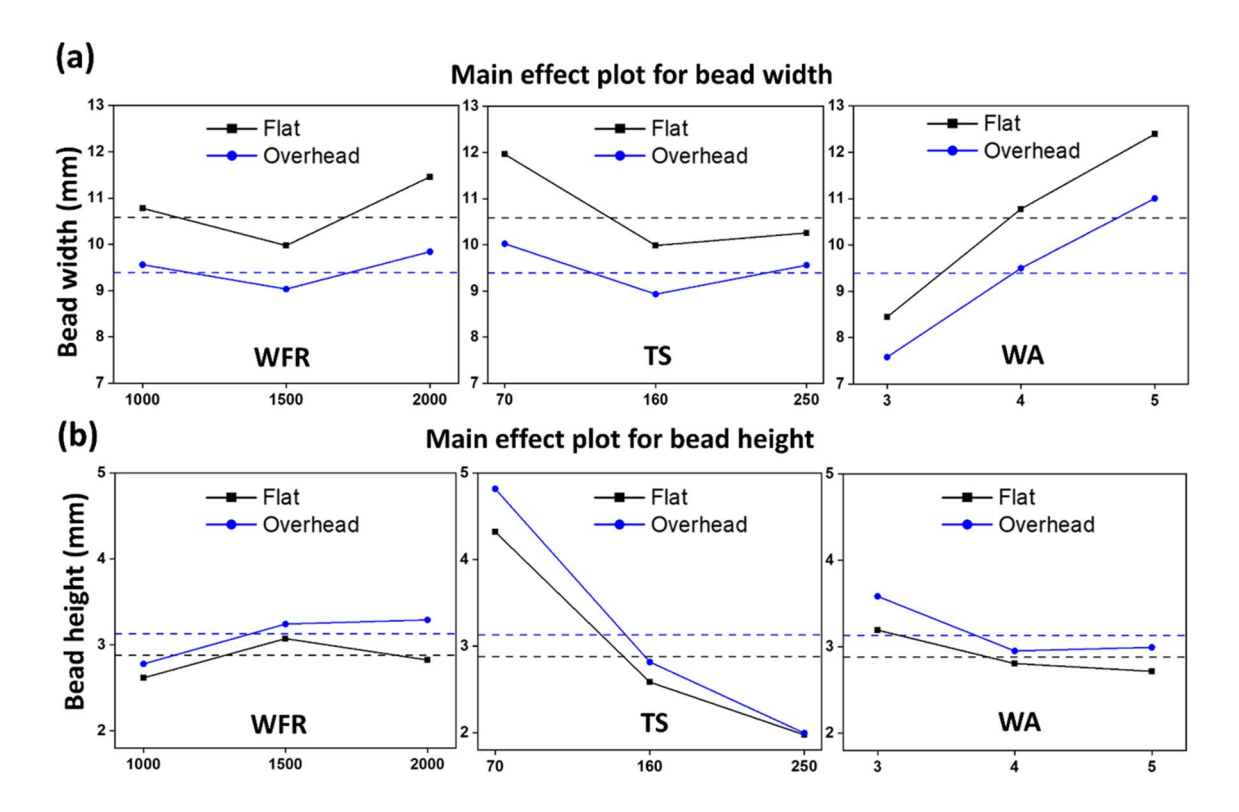


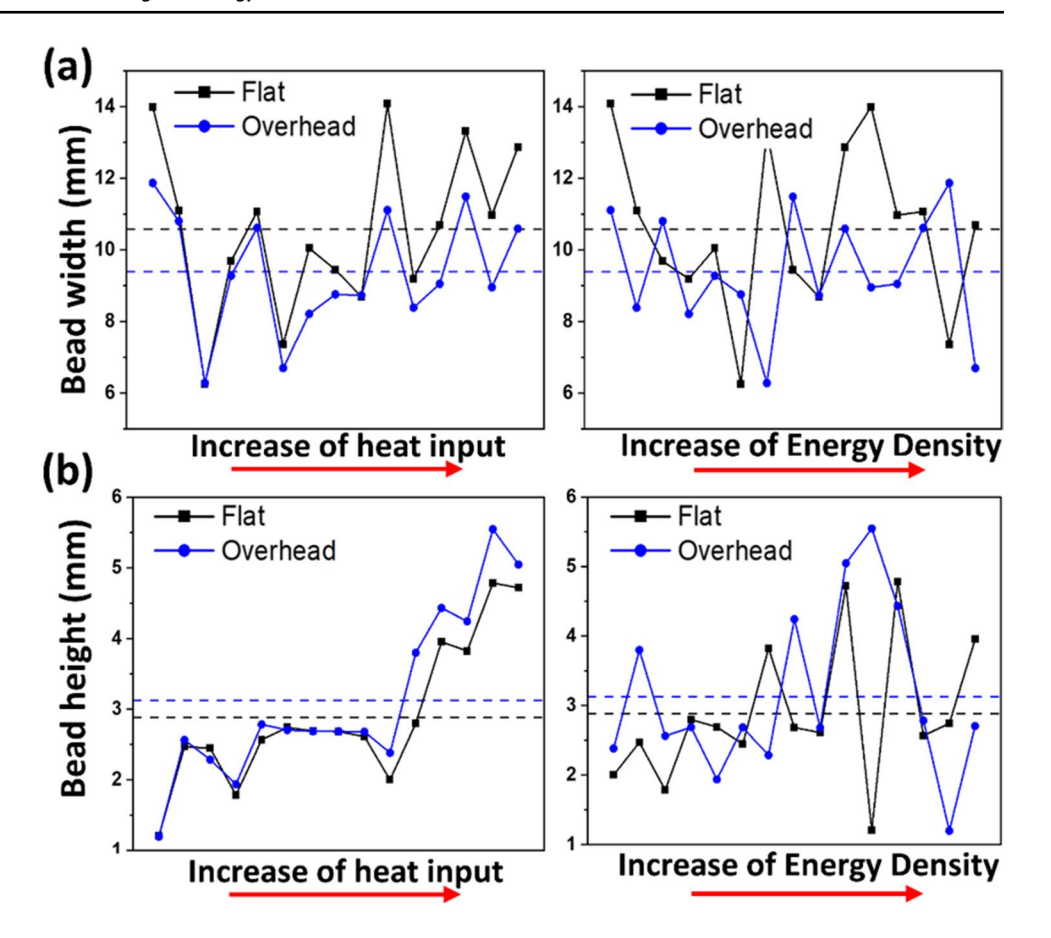
Fig. 2 ANOVA results showing a significant correlation among factors, factor levels, and responses for the overhead position

values. However, from layer 3 and onwards, increased fluctuations in the current and voltage value are found. The number of peaks and value of peak current increases as more layers are added. As the deposition proceeds the width of previously deposited layer gets reduced due

to sagging of molten metal due to gravity. This leads to increase in CTWD at sides of thin wall. In CMT process with increase in CTWD, more current will be required to melt the wire, which causes increase in number of peaks (fluctuation) and value of peak current. Increase in CTWD



Fig. 3 Effect of heat input and energy density on the bead width and bead height



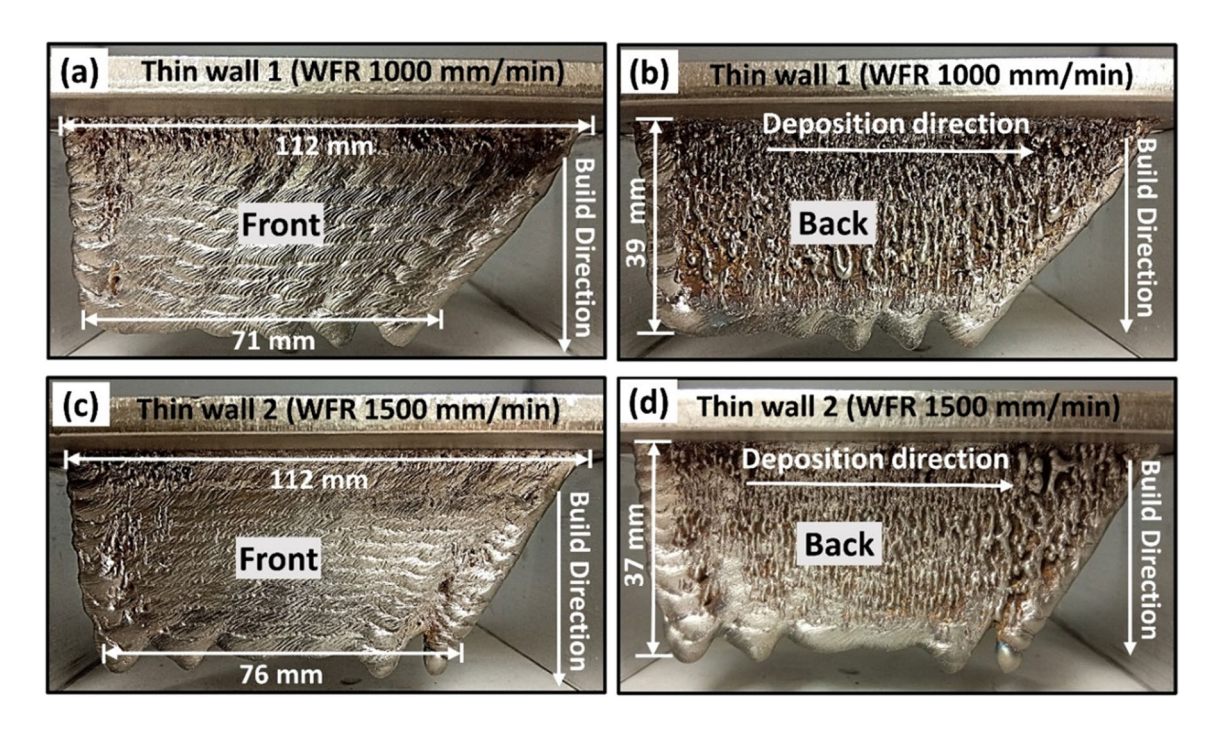


Fig. 4 Images of Thin-wall 1 (a) left and (b) right side, and Thin-wall 2 (c) left and (d) right side

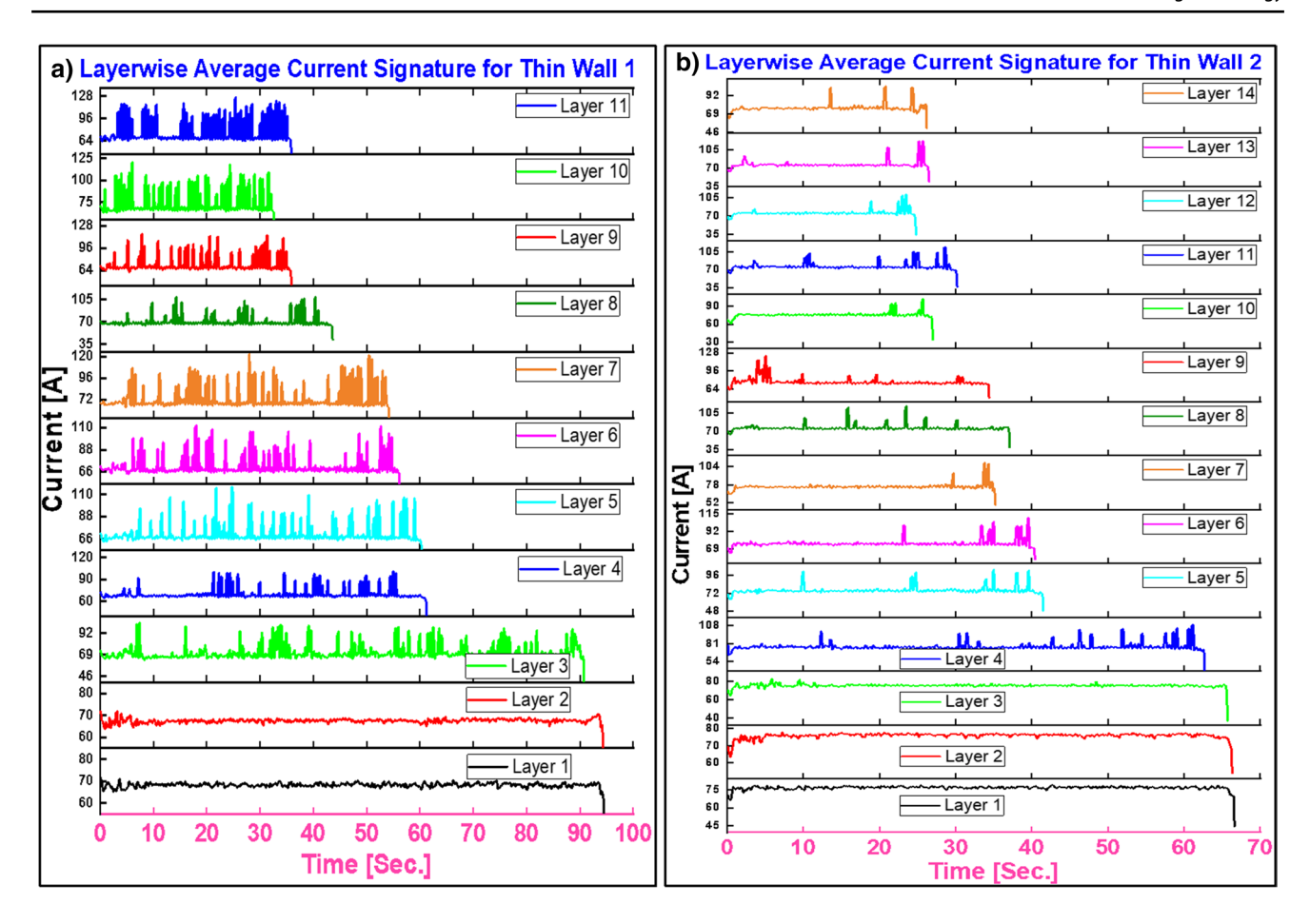


Fig. 5 The layer-wise current signatures for (a) Thin-wall 1 and (b) Thin-wall 2

at sides of thin wall also increases spatters at sides of thin wall, subsequently it affects the surface finish of thin wall. In case of thin-wall 2, fluctuation in the current signature starts from layer number 4 and continues to increase as new layers are added. However, for thin-wall 2 total peaks and drops are less prominent when compared with the current signature of the thin-wall 1.

Figure 6 shows the layer-wise average voltage signature for the two thin-walls. For both cases, the voltage varied within the range of 10 V-15 V. Fluctuations in voltage are less prominent at the bottom layers. It increases with the increase of build height. For thin-wall 1, there is more fluctuation in the average voltage as evidenced by sharp peaks and drops. This is consistent with the current signature, as variation in current will affect the voltage. In both cases, as the number of layers increases, the total deposition time decreases. This occurs because the top of the deposit is shorter than the bottom.

# 5.2 Surface roughness

To quantify the surface roughness, the walls were scanned using Hexagon 7725SEI-4 Roamer Absolute Arm, a portable coordinate measuring machine (CMM) equipped with PCD-MIS software. PCDMIS software stores the 3D geometry of the walls in a point cloud format. The results are summarized in Fig. 7. This file is then imported into the Cloud Compare software to be segmented, sliced, and reoriented. Then the processed file is saved as a.txt file. A MATLAB program is used to compute the surface roughness of both sides. MATLAB program processes the.txt file, fits the planes to both sides of the wall, and computes the deviation of points on the sides from the fitted plane. Finally, surface roughness is calculated using Eq. 3.

$$Surface\ Roughness(Ra) = \frac{\sum d_i}{N},\tag{3}$$



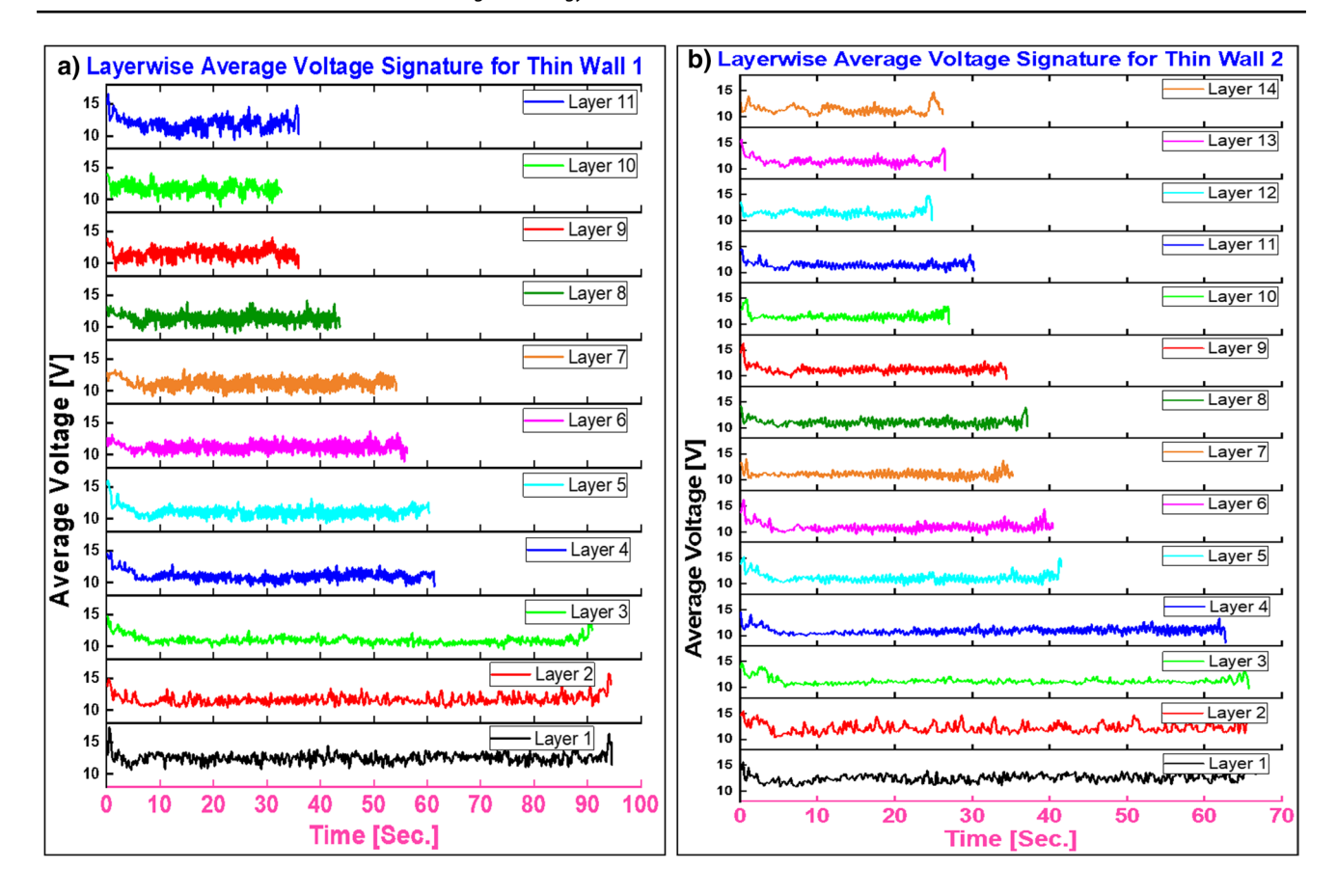


Fig. 6 The layer-wise voltage signatures for (a) Thin-wall 1 and (b) Thin-wall 2

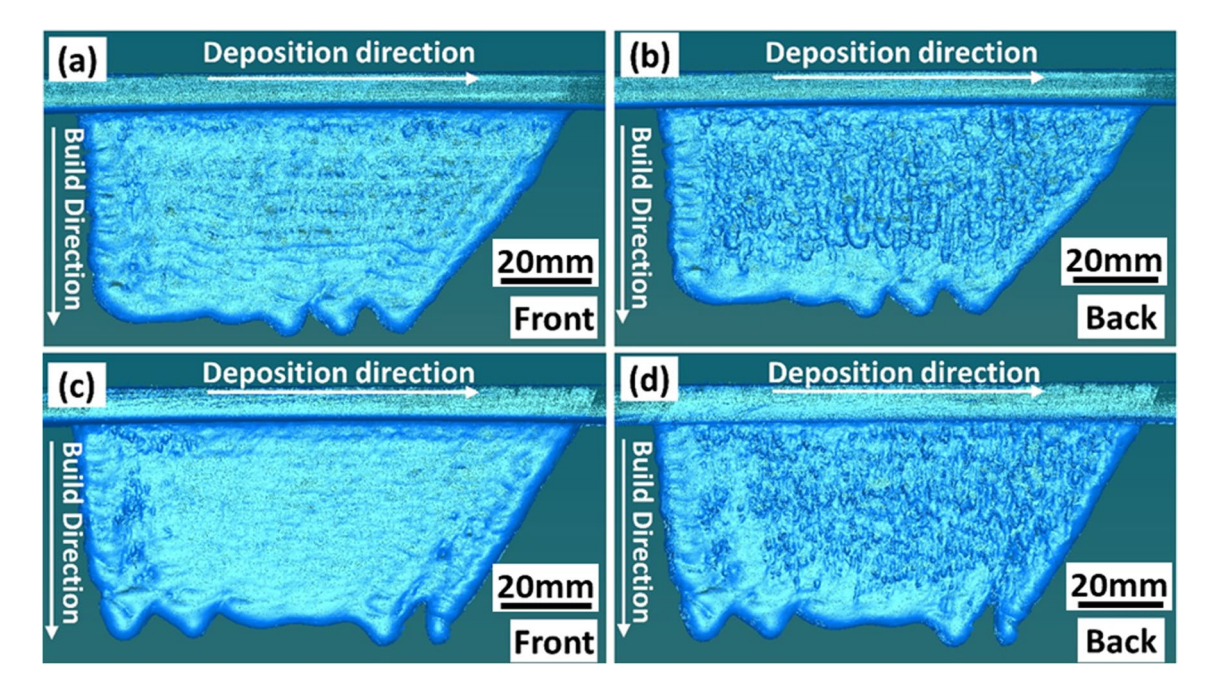


Fig. 7 CMM scanned data points showing front and back side of the overhead thin-wall 1(a-b) and thin-wall 2(c-d)



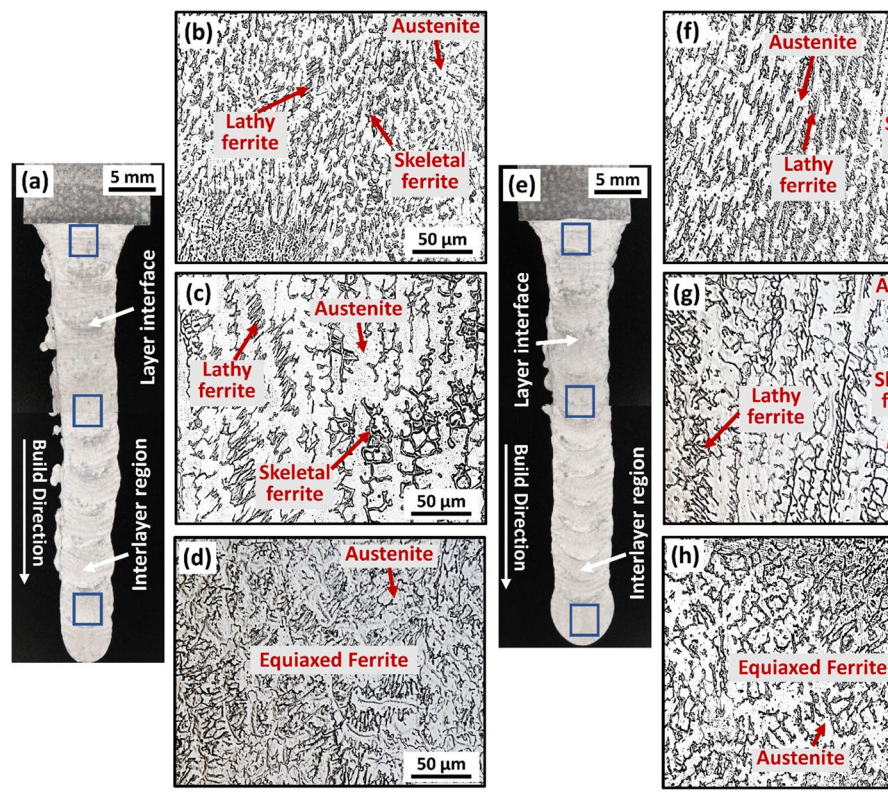
where  $d_i$  is the deviation of the point on the wall from the fitted plane, and N is the number of points.

Table 7 shows average surface roughness results for the deposited overhead structure. As the surface morphology is different on both side of the walls, it has been measured individually for each side for comparison. Surface roughness is 0.1748 mm and 0.4073 mm for front and backside respectively in thin-wall 1. It has been found 0.2091 mm and 0.2414 mm for thin-wall 2. From the results, it is confirmed that, surface roughness is lower at the front side in both of the deposits. In addition, the average surface roughness is larger for thin-wall 1 compared to thin-wall 2. This can be attributed to the more fluctuation in current and voltage signatures for thin-wall 1 due to reduction in bead width and increase in CTWD as compared to thin-wall 2 during layer by layer deposition. As discussed in Section 5.1 increase in CTWD at sides of thin wall also increases spatters at sides of thin wall, as the deposition process progresses which leads to increased surface roughness.

Table 7 Surface roughness results for overhead structure

Thin-wall	Front side ( <i>R<sub>a</sub></i> ) mm	Back side (R <sub>a</sub> ) mm	Average mm
1	0.1748	0.4073	0.2911

Fig. 8 OM images of (a–d) Thin-wall 1, e–h Thin-wall 2



#### 5.3 Microstructure

Figure 8a and e shows the OM images of the overall cross section of the deposits. Layer interface and interlayer regions could be identified due to the distinct morphology. For both walls, OM images were taken at the bottom, middle, and top of the deposit to characterize location dependent microstructure. Columnar grains are formed along the build direction. For each of the locations primary phase is the austenite  $(\gamma)$ where delta ( $\delta$ ) ferrite phase is segregated as dendrites. Figure 8b shows the microstructure of the bottom layer of the deposit. As the layer is close to the substrate, heat transfer is very high leading to the formation of finer dendrites. As new layers are added, there is temperature buildup in the deposit. As a result, coarse columnar dendrites are formed as shown in Fig. 8c. However, at the top layer equiaxed dendrites are formed. This layer does not undergo thermal cycles, can be considered as the rapid solidification microstructure of 316L due to the faster cooling rate. At the bottom and middle section of the deposit, delta ferrite consists of mainly lathy and skeletal ferrite. A similar morphology is found in thin-wall 2 as shown in Fig. 8f-h. Although according to pseudo-binary phase diagram of Fe-Cr-Ni at 70% Fe, only austenitic microstructure should be formed. However, due to non-equilibrium thermal cycle, repeated melting, and rapid cooling,  $\delta$  ferrites are retained in the final microstructure [40]. Similar microstructure is found in the literature for WAAM SS 316L [41, 42].



To study the morphological variation between the layer interface and interlayer region, OM and SEM analysis was performed and the results are shown in Fig. 9. The red line shows the interlayer boundary which separates both regions. The interlayer region consists of columnar dendrites, characteristics of the WAAM process. The layer interface region consists of equiaxed  $\delta$  ferrite in the  $\gamma$  matrix as shown in Fig. 9b and e. During the deposition of a new layer, some of the previous layer gets remelted due to the thermal cycle. This causes the  $\delta$  ferrite to dissolve in the austenite matrix, leading to the formation of equiaxed dendrites [43, 44]. Figure 9g–j shows SEM images of the layer interface and interlayer regions for both thin walls. Similar characteristics are also observed in these images.

#### 5.4 Microhardness

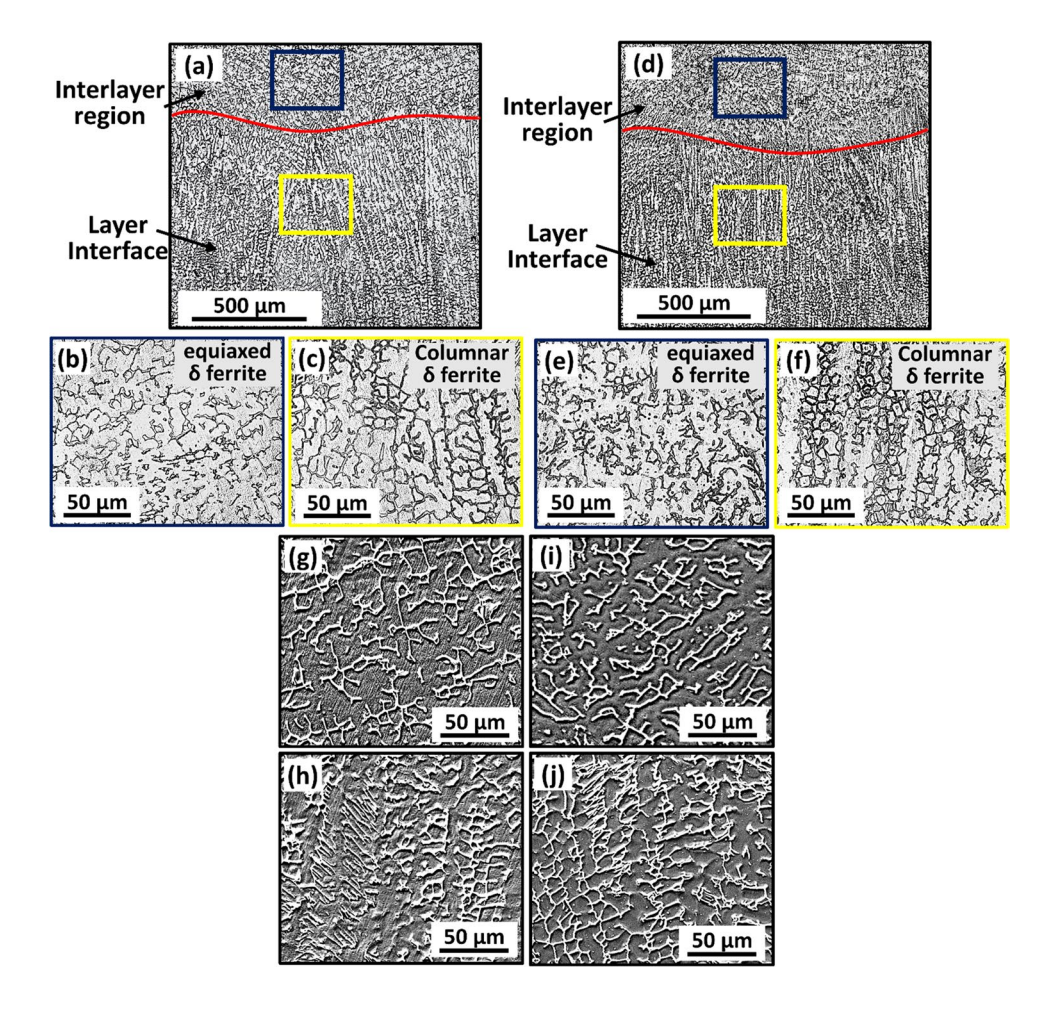
Figure 10a shows the microhardness profile of the overhead thin-walls from the substrate to the top of the thin-walls (with a spacing of 1 mm). The hardness values are in the range of 165–200 HV. The average hardness for Thin-wall 1 and 2 is 183 HV and 187.4 HV, respectively. No significant difference in hardness is observed between them. The

fluctuations in the hardness values over the deposit length may be due to the microstructural changes at the layer interface and inter-layer regions. Figure 10b shows that the average hardness of the thin-walls is less than ASTM A240-20 / ASTM A666-15 Annealed SS 316L [45, 46].

#### 5.5 Tensile test

Figure 11a and b show the stress-strain curves of overhead thin-walls, and Fig. 11c shows the location of specimens for microstructure and mechanical property investigation. Two vertical and two horizontal samples have been prepared from each of the thin-wall. For thin-wall 1, vertical and horizontal samples are named (V1, V2) and (H1, H2). Similarly, for thin-wall 2, vertical and horizontal samples are named (V3, V4) and (H3, H4). The results of the tensile test are summarized in Table 8. The UTS of V1 to V4 is 564, 570, 591, and 592 MPa. Their corresponding YS is 393, 370, 435, and 420 MPa, respectively. In the case of H1 to H4, UTS has been measured 597, 596, 569, and 605 MPa, and their YS is measured 374, 356, 393, and 406 MPa, respectively. The elongation of V1 to V4 is 46, 42, 48, and 44%, and for H1 to H4, it is 52, 69, 43, and

Fig. 9 Layer interface and interlayer region in overhead structure: **a-c**, **g**, **h** thin-wall 1, **d-f**, **i**, **j** thin-wall 2





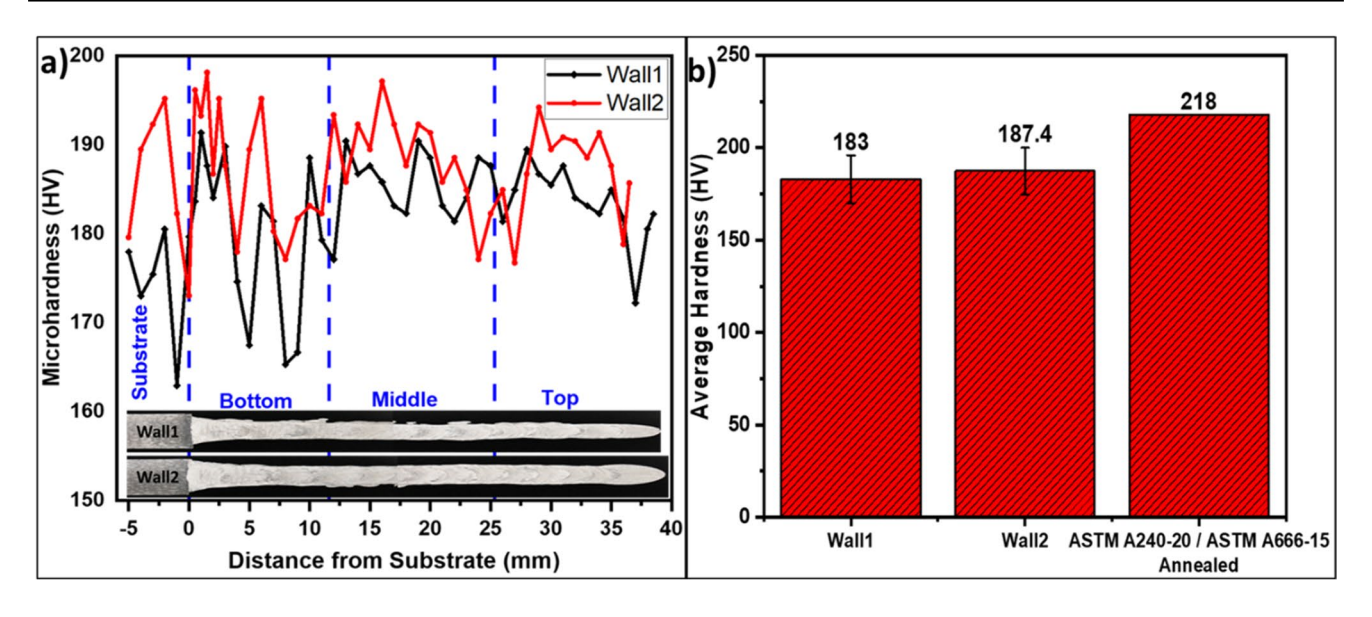


Fig. 10 a Microhardness profile of the substrate and thin-walls and (b) comparison of average microhardness of Thin-wall 1, Thin-wall 2, and annealed SS 316L

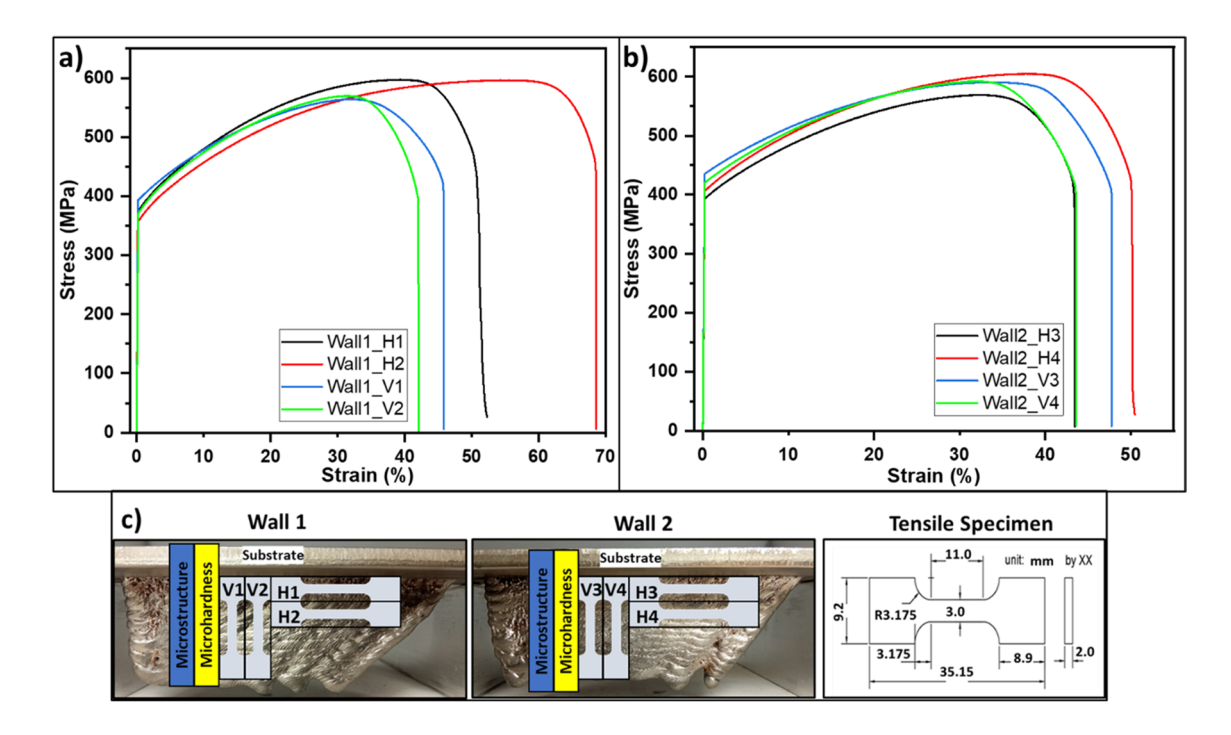


Fig. 11 Engineering stress-strain curves for (a) Thin-wall 1, b Thin-wall 2, and (c) location of microstructure, microhardness, and tensile specimen and the dimensions

50%. The highest UTS and YS have been found in H4 and V4 respectively. The average UTS and YS of vertical tensile specimens of thin-wall 2 were greater than that of thin-wall 1. Overall, there is considerable variation in UTS and YS in horizontal and vertical tensile specimens. This phenomenon exemplifies the existence of apparent anisotropy in mechanical properties between the horizontal

and vertical directions. This can be attributed to the non-equilibrium thermal cycles in the WAAM process.

# 5.6 Fractography

Figure 12 shows the fracture morphology of the tensiletested specimen. Lower magnification images show the



**Table 8** Summary of the tensile test results for different conditions

	Thin-wall 1				Thin-wall 2							
	H1	H2	Avg.	V1	V2	Avg.	Н3	H4	Avg.	V3	V4	Avg.
YS (MPa)	374	356	365	393	370	381.5	393	406	399.5	435	420	427.5
UTS (MPa)	597	596	596.5	564	570	567	569	605	587	591	592	591.5
Elongation (%)	52	69	60.5	46	42	44	43	50	46.5	48	44	46

overall fracture surface of samples. It is evident that, the samples went through severe plastic deformation before fracture. The marked region is shown at higher magnification for better understanding of the fracture characteristics. It is found that dimples with tearing edges are uniformly distributed over fractured surfaces, which confirms that ductile fracture has occurred. There is presence of void in the fracture surface as shown in V1 and V2. Cleavage facets are also present which are caused by the coalescence of

small dimples. In addition, many second-phase spherical particles are observed in fractured vertical and horizontal samples as marked by white area. Spherical particles were observed on the fracture surface which were identified as  $\delta$ -ferrite. These particles hinder the dislocation movement and induces dislocation buildup during the applied load [47]. However, no significant difference is observed in fracture morphology among the samples as the fracture mode is very similar.

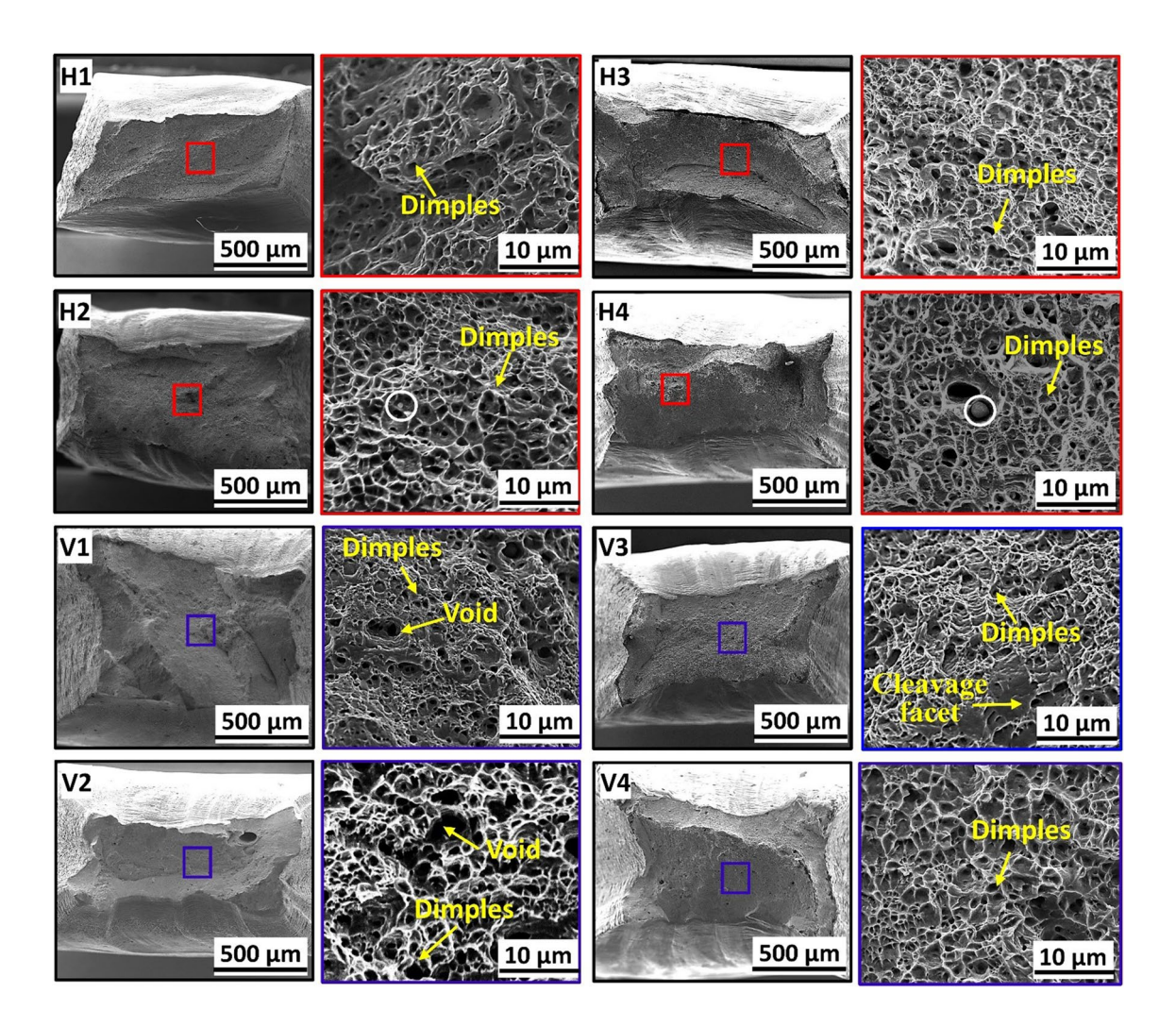


Fig. 12 Fracture morphology of tensile specimens; thin-wall 1 (H1, H2, V1, V2) and thin-wall 2 (H3, H4, V3, V4)

# 6 Discussion

# 6.1 Weld pool and bead geometry

COMSOL Multiphysics software (version 5.6) has been implemented to analyze the behavior of a weld pool in both flat and overhead positions. The electric currents, magnetic fields, laminar flow, and heat transfer modules are utilized for the simulation. Since the primary focus of this analysis is to study the behavior of the weld pool, the

arc plasma is not considered in the analysis. The modeling is performed to resemble the bead shape based on experimental findings. Steady-state condition is assumed in order to perform three-dimensional numerical modeling more efficiently. The thermal properties of SS 316L, required for the simulation have been collected from the literature [48]. Boundary conditions for heat flux, arc pressure [49], current density [50], and arc drag force [51] are set on the upper surface of the bead. Considering the weight percentage of sulfur (S) in SS 316L from Table 1, the Marangoni

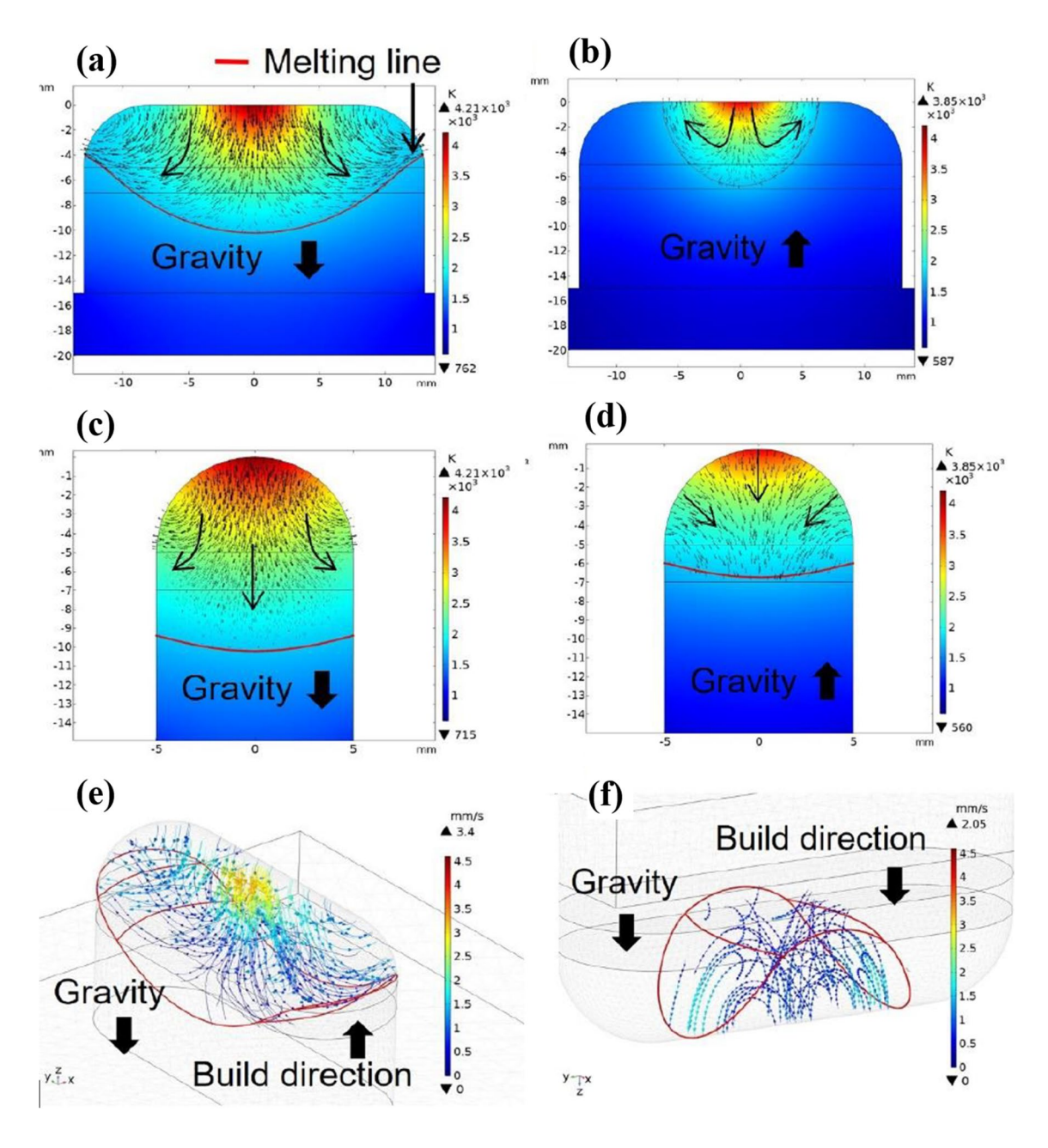


Fig. 13 Weld pool simulation, including temperature distribution and flow vector for (a, c, and e) flat and (b, d, and f) overhead position. Melting line, gravity, and build direction are shown with arrows



effect [52] and pressure due to surface tension [53] are also applied. Electromagnetic, buoyancy [53], and gravity are also defined within the weld pool as volume forces. In the flat position, the weld pool spreads downward from the center, and the maximum radius and depth of weld penetration are delineated by the melting line, as depicted in Fig. 13a and c. Conversely, in the overhead position, as illustrated in Fig. 13b and d, the weld pool tends to be narrower and smaller in comparison to the flat position. This behavior is primarily influenced by forces accelerated in the direction of gravity, wherein arc pressure, Marangoni flow, and surface tension emerge as the most significant factors. Figure 13c and f illustrate the weld pool as a three-dimensional streamline, showcasing its behavior in flat and overhead positions. In the overhead position, the tail of the weld pool increases in vertical direction due to reverse gravity paired with the backward flow, forming a convex bead shape.

Experiments C2, C4, C10, C11, and C15 resulted in abnormal beads, as shown in Table 5. Based on the observations, the most significant contributing factor in forming abnormal beads in all these experiments is the low WRF/TS ratio (<8), which reduces the volume of material deposited per unit of time. The other factors include dwell time and WA (in experiments C2 and C11). Due to dwell time, the welding torch stops on the sides for 0.1 s, which causes the weld metal accumulation. Figure 14 compares bead width and height in single-layer bead deposition for the overhead and flat positions. Overall, for the same experimental conditions, the bead width is greater in the flat position, and the bead height is larger in the overhead position. The weld pool simulation results in Fig. 13 also

support these phenomena. As the same volume of material is deposited, there should be a vice-versa relationship between these two parameters to maintain conservation of mass. These findings are consistent with the results obtained in the literature [21].

#### 6.2 Microstructure of thin-walls

The thermal history, including non-equilibrium thermal cycles, determines the microstructure of the WAAM deposited structure [54]. From Fig. 8, it has been found that, the microstructure varies along the deposition height. This variation of microstructure in different layers of WAAM SS 316L can be explained by the solidification theory. The solidification velocity (V) and temperature gradient (G) are the most influential parameters that control microstructure [55, 56]. At the beginning of the deposition process (initial layers), the temperature of the substrate is relatively low. This can result in a significant temperature gradient between the as-deposited layers and the substrate, which causes a high G/V ratio. As a result, columnar dendrites usually grow in the build direction [57]. As new layers are deposited, temperature buildup reduces the G/V ratio and coarse columnar dendrites are formed. The final layers do not go through significant remelting and the heat transfer is higher; leading to equiaxed dendrites. Similar findings have been reported in the literature [47].

#### 6.3 Mechanical properties of thin-walls

For both walls, it was observed that at 0.5–2 mm from the substrate, the hardness was in the range of 190–200 HV

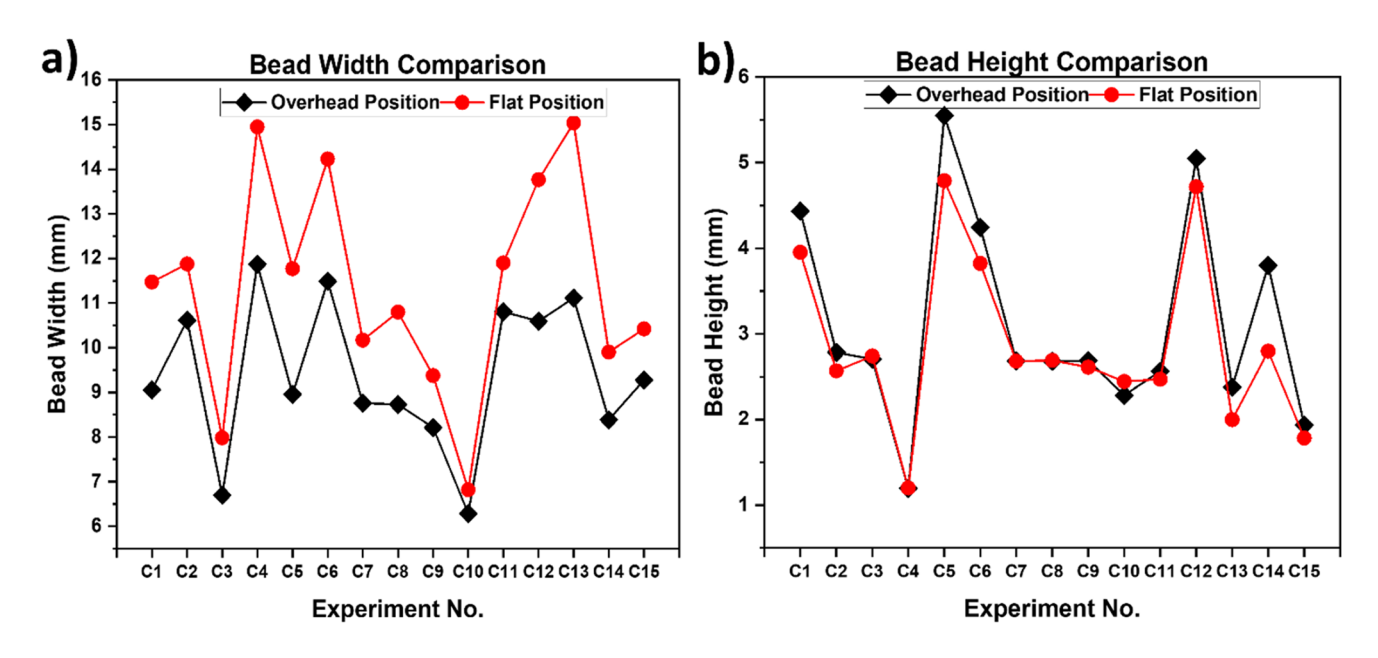
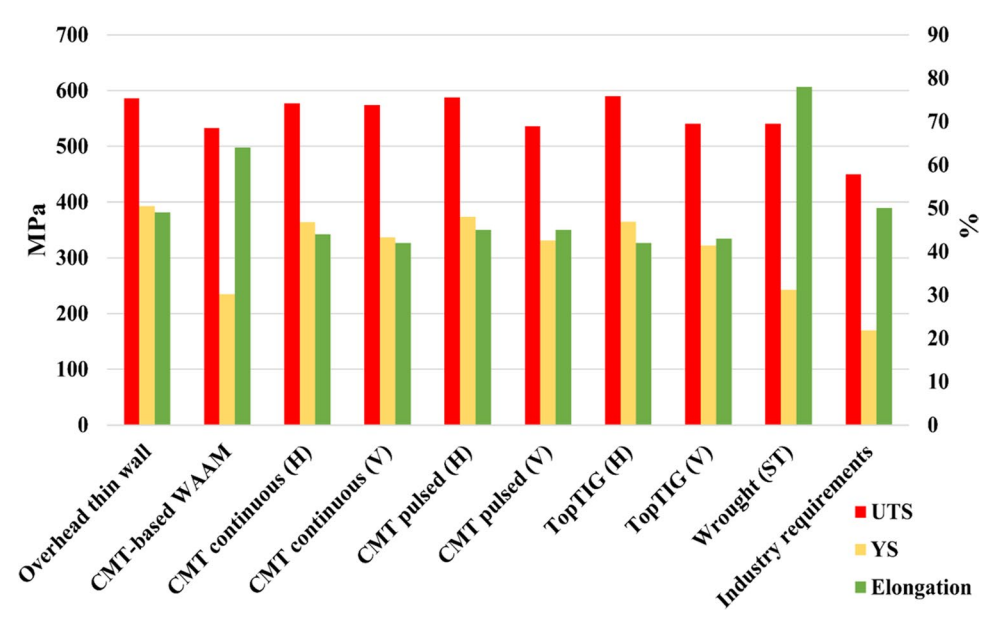


Fig. 14 Comparison of bead (a) width and (b) height in single-layer bead deposition for the overhead and flat positions

**Fig. 15** Comparison of tensile properties and elongation of the overhead thin-wall with the literature (H: Horizontal, V: Vertical, ST: Solution treated) [44, 57–60]



(Fig. 10a). This can be attributed to the higher cooling rate of the first layer. The higher cooling rate results in finer grain which promotes greater hardness [58]. Figure 15 compares the tensile properties of the overhead thin-wall with previously reported tensile properties of SS 316L fabricated by different manufacturing processes. The results are summarized in Table 9. As the mechanical properties varied due to anisotropy in overhead structure, average values of YS, UTS, and elongation were considered for comparison. The average YS of overhead thin-walls of SS 316L manufactured by CMT-WAAM structure is 393 MPa, which is higher than other techniques. UTS is 586 MPa, only TopTIG(H) and CMT pulse (H) has a larger value. The elongation value is 49%, higher than CMT continuous, CMT pulsed, and TopTIG processes. The commercial criterion for the tensile strength of wrought SS 316L is 525-623 MPa [59]. Therefore, the UTS of the overhead thin-walls lies in this range. Mechanical property mainly depends on the microstructure. Since the microstructure in overhead structure is

**Table 9** Room temperature mechanical property comparison for SS 316L

Process	UTS (MPa)	YS (MPa)	Elongation (%)
Overhead thin-wall	586	393	49
CMT-based WAAM	533	235	64
CMT continuous (H)	577	364	44
CMT continuous (V)	574	337	42
CMT pulsed (H)	588	374	45
CMT pulsed (V)	536	331	45
TopTIG (H)	590	365	42
TopTIG (V)	540	322	43
Wrought (ST)	540	242	78
Industry requirements	450	170	50

similar to other WAAM process, the results are also close to each other.

#### 7 Conclusion

This study investigated the feasibility of CMT-WAAM process to fabricate overhead thin-wall structure. It also analyzed the effect of the overhead deposition strategy on the geometry, surface roughness, microstructure, and mechanical properties of the single-layer beads and the thin-walls. The conclusions are as follows:

- The CMT-WAAM process can successfully fabricate overhead thin-walls of SS316L without the requirement of any support structure. No microstructural defects (e.g. cracks and porosity) were found in the microstructure.
- For single layer bead experiments in flat and overhead position, out of all process parameters, the weave amplitude is the most significant parameter on bead width, whereas travel speed is most significant parameter for bead height.
- Surface roughness is higher for thin-wall 1 which can be attributed reduction in bead width, increase in CTWD as the deposition proceeds.
- The microstructure of the overhead thin-wall consists of primary γ phase and δ ferrite are segregated in the microstructure. Different dendritic morphology is observed at different locations of the thin-wall.
- Average microhardness for thin-wall 1 and 2 is 183 HV and 187.4 HV respectively. The values are less than that of ASTM A240-20/ASTM A666-15 Annealed SS 316L.



 Tensile test properties are comparable to those reported in previous literature. Higher elongation values and a large number of dimples on the fracture surface suggest ductile failure occurred during the tensile test.

The authors plan to expand this work by further investigating the computational modeling to elucidate the underlying physics of the bead formation and the surface roughness of a thin-wall. Several influential factors on the bead formation and the thin-wall, such as (1) surface tension, (2) arc force, (3) droplet impact, (4) the normal force from the solidified part, (5) gravity, (6) buoyancy force, and (7) friction will be investigated.

Author contribution Sainand Jadhav: Writing – original draft, Validation, Methodology, Investigation. Gwang Ho Jeong: Writing – review & editing, Computational Modeling, Conceptualization. Mahdi Sadeqi Bajestani: Writing – review & editing, Investigation, Formal analysis. Saiful Islam: Writing – review & editing, Investigation. Ho-Jin Lee: Writing – review & editing, Conceptualization. Young Tae Cho: Writing – review & editing, Conceptualization. Duck Bong Kim: Writing – review & editing, Project administration, Funding acquisition, Conceptualization.

Funding This material is based upon work supported by the National Science Foundation under Grant No. 2015693. The authors of this paper appreciate the continuous support provided by the Center for Manufacturing Research (CMR) and the Department of Manufacturing and Engineering Technology at Tennessee Technological University.

#### **Declarations**

Conflicts of interest/competing interests The authors declare that they have no known competing financial interests or personal relationships that could have appeared to influence the work reported in this paper.

#### References

- Mostafaei A, Ghiaasiaan R, Ho I-T, Strayer S, Chang K-C, Shamsaei N, Shao S, Paul S, Yeh A-C, Tin S, To AC (2023) Additive manufacturing of nickel-based superalloys: a state-of-the-art review on process-structure-defect-property relationship. Prog Mater Sci 136:101108. https://doi.org/10.1016/j.pmatsci.2023. 101108
- 2. ISO/ASTM 52900:2021(en) Additive manufacturing General principles Fundamentals and vocabulary. https://www.iso.org/obp/ui/#iso:std:iso-astm:52900:ed-2:v1:en
- Ahsan MRU, Tanvir ANM, Ross T, Elsawy A, Oh MS, Kim DB (2019) Fabrication of bimetallic additively manufactured structure (BAMS) of low carbon steel and 316L austenitic stainless steel with wire + arc additive manufacturing. Rapid Prototyp J 26:519–530. https://doi.org/10.1108/RPJ-09-2018-0235
- Mostafaei A, Zhao C, He Y, Reza Ghiaasiaan S, Shi B, Shao S, Shamsaei N, Wu Z, Kouraytem N, Sun T, Pauza J, Gordon JV, Webler B, Parab ND, Asherloo M, Guo Q, Chen L, Rollett AD (2022) Defects and anomalies in powder bed fusion metal additive manufacturing. Curr Opin Solid State Mater Sci 26:100974. https://doi.org/10.1016/j.cossms.2021.100974

- Frazier WE (2014) Metal additive manufacturing: a review.
   J Mater Eng Perform 23:1917–1928. https://doi.org/10.1007/ S11665-014-0958-Z/FIGURES/9
- Li Y, Su C, Zhu J (2022) Comprehensive review of wire arc additive manufacturing: hardware system, physical process, monitoring, property characterization, application and future prospects. Results Eng 13:100330. https://doi.org/10.1016/j. rineng.2021.100330
- Srivastava M, Rathee S, Tiwari A, Dongre M (2023) Wire arc additive manufacturing of metals: a review on processes, materials and their behaviour. Mater Chem Phys 294:126988. https:// doi.org/10.1016/j.matchemphys.2022.126988
- Tomar B, Shiva S, Nath T (2022) A review on wire arc additive manufacturing: Processing parameters, defects, quality improvement and recent advances. Mater Today Commun 31:103739. https://doi.org/10.1016/j.mtcomm.2022.103739
- Nycz A, Adediran AI, Noakes MW, Love LJ (2016) Large scale metal additive techniques review. Solid Free Fabr 2016 Proc 27th Annu Int Solid Free Fabr Symp - An Addit Manuf Conf SFF 2016:2001–2006
- Relativity Space nears launch of first 3D-printed rocket (n.d.) https:// mynews13.com/fl/orlando/news/2022/08/17/relativity-space-nearslaunch-of-first-3d-printed-rocket. Accessed 5 Aug 2023
- Lehmann T, Rose D, Ranjbar E, Ghasri-Khouzani M, Tavakoli M, Henein H, Wolfe T, Jawad Qureshi A (2022) Large-scale metal additive manufacturing: a holistic review of the state of the art and challenges. Int Mater Rev 67:410–459. https://doi.org/10.1080/09506608.2021.1971427
- Ding Y, Kovacevic R (2016) Feasibility study on 3-D printing of metallic structural materials with robotized laser-based metal additive manufacturing. JOM 68:1774–1779. https://doi.org/10. 1007/s11837-016-1929-7
- Chakkravarthy V, Jerome S (2020) Printability of multiwalled SS 316L by wire arc additive manufacturing route with tunable texture. Mater Lett 260:126981. https://doi.org/10.1016/j.matlet.2019.126981
- Xie B, Xue J, Ren X (2020) Wire arc deposition additive manufacturing and experimental study of 316L stainless steel by CMT + P process. Metals (Basel) 10(11):1419. https://doi.org/ 10.3390/met10111419
- Xiong J, Lei Y, Chen H, Zhang G (2017) Fabrication of inclined thin-walled parts in multi-layer single-pass GMAW-based additive manufacturing with flat position deposition. J Mater Process Technol 240:397–403. https://doi.org/10.1016/j.jmatprotec. 2016 10 019
- Panchagnula JS, Simhambhatla S (2015) Additive manufacturing of complex shapes through weld-deposition and feature based slicing. ASME Int Mech Eng Congr Expo Proc 2A-2015. https://doi.org/10.1115/IMECE2015-51583
- Zhao Y, Li F, Chen S, Lu Z (2020) Direct fabrication of inclined thin-walled parts by exploiting inherent overhanging capability of CMT process. Rapid Prototyp J 26:499–508. https://doi.org/ 10.1108/RPJ-03-2019-0081
- Li Y, Qin X, Wu Q, Hu Z, Shao T (2020) Fabrication of curved overhanging thin-walled structure with robotic wire and arc additive manufacturing (RWAAM). Ind Robot Int J Robot Res Appl 47:102–110. https://doi.org/10.1108/IR-05-2019-0112
- Baek S-Y, Nam J-H (2021) Physical welding factors for reclassified welding positions in shipbuilding assembly process based on muscle activity measured by surface electromyography. J Mar Sci Eng 9(11):1211. https://doi.org/10.3390/jmse9111211
- Nguyen MC, Medale M, Asserin O, Gounand S, Gilles P (2017) Sensitivity to welding positions and parameters in GTA welding with a 3D multiphysics numerical model. Numer Heat Transf Part A Appl 71:233–249. https://doi.org/10.1080/10407782.2016. 1264747



- Park J-H, Kim S-H, Moon H-S, Kim M-H (2019) Influence of gravity on molten pool behavior and analysis of microstructure on various welding positions in pulsed gas metal arc welding. Appl Sci 9(21):4626. https://doi.org/10.3390/app9214626
- Yaakub MY, Tham G, Abd Rahim WMAW, MohdRadzi MAR, Mahmud A (2013) Prediction of welding parameters and weld bead geometry for GMAW process in overhead T-fillet welding position(4F). Adv Mater Res 686:320–324. https://doi.org/10. 4028/www.scientific.net/AMR.686.320
- Kang N, Singh J, Kulkarni AK (2003) Effects of gravitational orientation on the microstructural evolution of gas tungsten arc welds in an Al-4 wt% Cu alloy. J Mater Sci 38:3579–3589. https:// doi.org/10.1023/A:1025617128625
- Kang N, Mahank TA, Kulkarni AK, Singh J (2003) Effects of gravitational orientation on surface deformation and weld pool geometry during gas tungsten arc welding. Mater Manuf Process 18:169–180. https://doi.org/10.1081/AMP-120018903
- 25. Hu Z, Hua L, Qin X, Ni M, Ji F, Wu M (2021) Molten pool behaviors and forming appearance of robotic GMAW on complex surface with various welding positions. J Manuf Process 64:1359–1376. https://doi.org/10.1016/j.jmapro.2021.02.061
- Murphy AB (2013) Influence of droplets in gas—metal arc welding: new modelling approach, and application to welding of aluminium. Sci Technol Weld Join 18:32–37. https://doi.org/10.1179/1362171812Y.0000000069
- Ogino Y, Hirata Y (2015) Numerical simulation of metal transfer in argon gas-shielded GMAW. Weld World 59:465–473. https:// doi.org/10.1007/s40194-015-0221-8
- Ogino Y, Hirata Y, Murphy AB (2016) Numerical simulation of GMAW process using Ar and an Ar–CO2 gas mixture. Weld World 60:345–353. https://doi.org/10.1007/s40194-015-0287-3
- Zhao Y, Chung H (2017) Numerical simulation of droplet transfer behavior in variable polarity gas metal arc welding. Int J Heat Mass Transf 111:1129–1141. https://doi.org/10.1016/j.ijheatmass transfer.2017.04.090
- Zhao W, Wei Y, Long J, Chen J, Liu R, Ou W (2021) Modeling and simulation of heat transfer, fluid flow and geometry morphology in GMAW-based wire arc additive manufacturing. Weld World 65:1571–1590. https://doi.org/10.1007/s40194-021-01123-1
- Wang X, Huang Y, Zhang Y (2013) Droplet transfer model for laser-enhanced GMAW. Int J Adv Manuf Technol 64:207–217. https://doi.org/10.1007/s00170-012-4014-6
- Haidar J, Lowke JJ (1996) Predictions of metal droplet formation in arc welding. J Phys D Appl Phys 29:2951. https://doi.org/10. 1088/0022-3727/29/12/003
- Choi JH, Lee J, Yoo CD (2001) Dynamic force balance model for metal transfer analysis in arc welding. J Phys D Appl Phys 34:2658. https://doi.org/10.1088/0022-3727/34/17/313
- Dordlofva C, Törlind P (2020) Evaluating design uncertainties in additive manufacturing using design artefacts: Examples from space industry. Des Sci 6. https://doi.org/10.1017/dsj.2020.11
- Chen H, Yaseer A, Zhang Y (2022) Top surface roughness modeling for robotic wire arc additive manufacturing. J Manuf Mater Process 6(2):39. https://doi.org/10.3390/jmmp6020039
- Ding D, He F, Yuan L, Pan Z, Wang L, Ros M (2021) The first step towards intelligent wire arc additive manufacturing: an automatic bead modelling system using machine learning through industrial information integration. J Ind Inf Integr 23:100218 https://api.semanticscholar.org/CorpusID:233649154
- Yehorov Y, da Silva LJ, Scotti A (2019) Balancing WAAM production costs and wall surface quality through parameter selection: a case study of an Al-Mg5 alloy multilayer-non-oscillated single pass wall. J Manuf Mater Process 3(2):32. https://doi.org/10.3390/jmmp3020032
- 38. Li B, Wang B, Zhu G, Zhang L, Lu B (2021) Low-roughnesssurface additive manufacturing of metal-wire feeding with small

- power. Materials (Basel) 14:1-17. https://doi.org/10.3390/ma14154265
- Selvi S, Vishvaksenan A, Rajasekar E (2018) Cold metal transfer (CMT) technology An overview. Def Technol 14:28–44. https://doi.org/10.1016/j.dt.2017.08.002
- Jafarzad-Shayan MM, Zarei-Hanzaki A, Moshiri A, Seop Kim H, Haftlang F, Tahaghoghi M, Mahmoudi M, Momeni M, Abedi HR (2023) Microstructural heterogeneity and exceptional mechanical properties in a wire-arc additively manufactured stainless steel. Mater Sci Eng A 882:145473. https://doi.org/ 10.1016/j.msea.2023.145473
- Senthil TS, Babu SR, Puviyarasan M, Balachandar VS (2023) Experimental investigations on the multi-layered SS316L wall fabricated by CMT-based WAAM: Mechanical and microstructural studies. J Alloy Metall Syst 2:100013. https://doi.org/10. 1016/j.jalmes.2023.100013
- 42. Gowthaman PS, Jeyakumar S, Sarathchandra D (2023) Effect of heat input on microstructure and mechanical properties of 316L stainless steel fabricated by wire arc additive manufacturing. J Mater Eng Perform. https://doi.org/10.1007/ s11665-023-08312-7
- Vora J, Parmar H, Chaudhari R, Khanna S, Doshi M, Patel V (2022) Experimental investigations on mechanical properties of multi-layered structure fabricated by GMAW-based WAAM of SS316L. J Mater Res Technol 20:2748–2757. https://doi.org/10.1016/j.jmrt.2022.08.074
- Chen X, Li J, Cheng X, He B, Wang H, Huang Z (2017) Microstructure and mechanical properties of the austenitic stainless steel 316L fabricated by gas metal arc additive manufacturing. Mater Sci Eng A 703:567–577. https://doi.org/10.1016/j.msea.2017.05. 024
- American Society for Testing and Materials (2004) ASTM A240: Standard Specification for Chromium and Chromium-Nickel Stainless Steel Plate, Sheet, and Strip for Pressure Vessels and for General Applications. ASTM Int I:12. https://doi.org/10.1520/ A0240
- ASTMA666-15 (2015) Standard Test; Specification for Annealed or Cold-Worked Austenitic StainlessSteel Sheet, Strip, Plate, and Flat Bar. ASTM Int: 1–7. https://doi.org/10.1520/A0666-23.2
- Long P, Wen D, Min J, Zheng Z, Li J, Liu Y (2021) Microstructure evolution and mechanical properties of a wire-arc additive manufactured austenitic stainless steel: Effect of processing parameter. Materials (Basel) 14(7):1681. https://doi.org/10.3390/ma140 71681
- 48. Traidia A (2011) Multiphysics modelling and numerical simulation of GTA weld pools, PhD diss., Ecole Polytechnique X. https://pastel.hal.science/pastel-00709055/
- Cho D-W, Park J-H, Moon H-S (2019) A study on molten pool behavior in the one pulse one drop GMAW process using computational fluid dynamics. Int J Heat Mass Transf 139:848–859. https://doi.org/10.1016/j.ijheatmasstransfer.2019.05.038
- Kou S, Sun DK (1985) Fluid flow and weld penetration in stationary arc welds. Metall Trans A 16:203–213. https://doi.org/10.1007/BF02815302
- Cheon J, Kiran DV, Na S-J (2016) CFD based visualization of the finger shaped evolution in the gas metal arc welding process. Int J Heat Mass Transf 97:1–14. https://doi.org/10.1016/j.ijheatmass transfer.2016.01.067
- Sahoo P, Debroy T, McNallan MJ (1988) Surface tension of binary metal—surface active solute systems under conditions relevant to welding metallurgy. Metall Trans B 19:483–491. https://doi.org/ 10.1007/BF02657748
- Cho W-I, Na S (2021) Impact of driving forces on molten pool in gas metal arc welding. Weld World 65:1735–1747 https://api. semanticscholar.org/CorpusID:234476295



- 54. Jin W, Zhang C, Jin S, Tian Y, Wellmann D, Liu W (2020) Wire arc additive manufacturing of stainless steels: a review. Appl Sci 10(5):1563. https://doi.org/10.3390/app10051563
- Kou S (2002) Welding metallurgy. Weld Metall. https://doi.org/ 10.1002/0471434027
- Song B, Zhao X, Li S, Han C, Wei Q, Wen S, Liu J, Shi Y (2015)
   Differences in microstructure and properties between selective laser melting and traditional manufacturing for fabrication of metal parts: a review. Front Mech Eng 10:111–125. https://doi.org/10.1007/s11465-015-0341-2
- Wang L, Xue J, Wang Q (2019) Correlation between arc mode, microstructure, and mechanical properties during wire arc additive manufacturing of 316L stainless steel. Mater Sci Eng A 751:183–190. https://doi.org/10.1016/j.msea.2019.02.078
- Kirkpatrick CW, Benjamin D (1980) Properties and selection, stainless steels, tool materials, and special purpose metals. Am Soc Met 9

- Rodríguez NK, Vázquez L, Huarte I, Arruti E, Tabernero I, Álvarez P (2018) Wire and arc additive manufacturing: a comparison between CMT and TopTIG processes applied to stainless steel. Weld World 62:1083–1096 https://api.semanticscholar.org/Corpu sID:139627519
- ASTMA473-15 (2015) Standard specification for stainless steel forgings. ASTM Int: 1–5. https://doi.org/10.1520/A0473-13.2

**Publisher's Note** Springer Nature remains neutral with regard to jurisdictional claims in published maps and institutional affiliations.

Springer Nature or its licensor (e.g. a society or other partner) holds exclusive rights to this article under a publishing agreement with the author(s) or other rightsholder(s); author self-archiving of the accepted manuscript version of this article is solely governed by the terms of such publishing agreement and applicable law.

